**Article:**

Chinelatto, A.L., Boulahya, K., Perez-Coll, D. et al. (6 more authors) (2015) Synthesis of a 12R-type hexagonal perovskite solid solution Sr3NdNb3-xTixO12-delta and the influence of acceptor doping on electrical properties. Dalton Transactions, 44 (16). pp. 7643-7653. ISSN 1477-9226

https://doi.org/10.1039/c5dt00170f

# Dalton Transactions

Accepted Manuscript

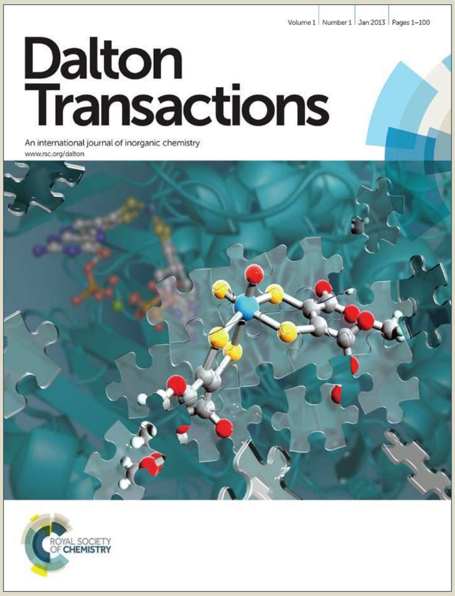

ROYAL SOCIETY OF CHEMISTRY

www.rsc.org/dalton

# Synthesis of a 12R-type Hexagonal Perovskite Solid Solution $Sr_3NdNb_{3-x}Ti_xO_{12-\delta}$ and the Influence of Acceptor Doping on Electrical Properties

Adilson L. Chinelatto[a,b], Khalid Boulahya[c], Domingo Pérez-Coll[a], Ulises Amador[d], Corina Tabacaru[a], Simon Nicholls[e], Markus Hoelzel[f], Derek C. Sinclair[e], Glenn C. Mather[a*]

[a] Instituto de Cerámica y Vidrio, CSIC, Cantoblanco,28049 Madrid, Spain
[b]Departamento de Engenharia de Materiais, Universidade Estadual de Ponta Grossa, Av. Gal. Carlos Cavalcanti, 4748, 84030-900- Ponta Grossa-PR, Brazil
[c]Departamento de Química Inorgánica I, Facultad de Ciencias Químicas, Universidad Complutense, Ciudad Universitaria, 28040 Madrid, Spain
[d]Facultad de Farmacia, Departamento de Química, Urbanización Monteprincipe, Universidad CEU San Pablo, Boadilla del Monte, 28668 Madrid, Spain
[e]Department of Materials Science & Engineering, Sir Robert Hadfield Building, University of Sheffield, Mappin Street, Sheffield S1 3JD, United Kingdom
[f] Forschungsneutronenquelle Heinz Maier-Leibnitz(FRM II),Technische Universität München, Lichtenbergstrasse 1, D-85747 Garching, Germany

*e-mail address: mather@icv.csic.es
Tel.: + 34 917355840
Fax.: + 34 917355843

## Abstract

A solid solution forms for $Sr_3NdNb_{3-x}Ti_xO_{12-\delta}$ with approximate limits $0 \le x \le 0.06$. The system crystallizes with a 12R-type hexagonal perovskite structure in space group $R\bar{3}$, as determined by neutron diffraction and selected area electron diffraction. The electrical properties of the end members have been investigated by impedance spectroscopy in the temperature range 550 – 800 °C in various gas atmospheres and as a function of oxygen and water-vapour partial pressure. Proton transport dominates in wet oxidising conditions in the temperature range 550 to 700 °C, as confirmed by the $H^+/D^+$ isotope effect. Acceptor doping considerably enhances proton conductivity with a value of $3.3 \times 10^{-6}$ $Scm^{-1}$ for the bulk response of x = 0.06 at 700 °C in moistened air. The presence of a – ¼ slope for both doped and undoped samples in the range $10^{-19} \le pO_2 \le 10^{-8}$ atm at 900 °C indicates n-type transport in reducing conditions following the extrinsic model attributable to acceptor centres. The conductivity is essentially independent of $pO_2$ at 600 °C in dry oxidising conditions, consistent with oxide-ion transport; a positive power-law dependence at higher temperature indicates extrinsic behaviour and a significant electron-hole contribution. The dielectric constant at RT of nominally stoichiometric $Sr_3NdNb_3O_{12}$ is $\varepsilon_r \sim 37$, with a moderately high quality factor of $Q \times f \sim 16400$ GHz at $f_r \sim 6.4$ GHz. The temperature coefficient of resonant frequency of x = 0 is $\tau_f$ ~ 12ppm/°C, which lowers to -3 ppm/°C for the Ti-doped phase x = 0.06.

**Keywords:** Proton conduction, microwave dielectric, crystal structure, acceptor centre, octahedral tilting, defect analysis

## 1. Introduction

Oxides derived from the perovskite structure ($ABO_3$) are probably the most widely studied class of compounds in solid-state chemistry. The ability of the perovskite structure to accommodate the majority of cations in the periodic table, with ranging compositions, leads to an extremely diverse array of physical properties, encompassing electrical, magnetic, dielectric, optical and catalytic applications.

Perovskites may be classified structurally according to close packing of the $AO_3$ layers. Cubic close packing (ccp) gives rise to the familiar cubic perovskite structure in which all $BO_6$ octahedra share corners. Hexagonal close packing (hcp) is characterised by face-sharing octahedra with the cation sites in close proximity. Different combinations of ccp and hcp stacking sequences with both corner- and face-sharing octahedra lead to a rich structural and compositional complexity within the hexagonal-perovskite family [1,2]. The nomenclature employed to describe the unit cells of the family members includes the number of $AO_3$ layers per cell and a symbol to describe the unit-cell symmetry.

Proton transport in perovskite oxides is of considerable interest for applications in high-temperature electrochemical devices such as proton-conducting solid oxide fuel cells (protonic ceramic fuel cells, PCFCs) and ceramic hydrogen-permeation membranes [3–5]. The best proton-conducting perovskites have large $A^{2+}$ and $B^{4+}$ cations, such as $Ba^{2+}$ and $Ce^{4+}$, and are doped on the B site with a lower valence cation (typically $Y^{3+}$) to form oxygen vacancies in the dry state. A number of interdependent factors involving the constituent cations and perovskite lattice have varying degrees of influence on the proton transport, including basicity, molar volume, tolerance factor and symmetry [3,4,6]. The key properties of high conductivity and good stability are, however, somewhat incompatible, making the search for better materials, including the exploration of other structure types [7], highly relevant. In this regard, we recently reported that modest proton conductivity is observed in humid, oxidising atmospheres for the 12R-type hexagonal perovskite $Sr_3LaNb_3O_{12}$ (12 $AO_3$ layers, rhombohedral symmetry) [8], which is, to our knowledge, the first report of proton transport in a cation-deficient perovskite, $A_xB_{1-x}O_{3x}$.

Whereas the use of perovskites in ion-conducting applications at high temperatures is very promising, their employment as dielectric materials in ambient conditions is critical to state-of-the-art electrical components such as tunable microwave devices, for which the required properties are moderate to high permittivity, low dielectric losses and negligible temperature variation of the resonant frequency ($\tau_f$ ~ 0 ppm /K) [9,10]. The structure-property relations of hexagonal perovskites, although less well understood than the ccp counterparts [11], are receiving increasing attention in this regard [12,13]. $Sr_3LaNb_3O_{12}$ has recently been investigated as a good low-loss dielectric material for resonators and filters [14,15]. Here again, the interplay among the polarisability of the constituent cations, tolerance factor and degree of octahedral tilting play fundamental roles in the observed properties [14,16].

In this paper, we have undertaken a first, wide-ranging study of the structural and electrical properties of the hexagonal perovskite $Sr_3NdNb_3O_{12}$. Neutron diffraction and selected area electron diffraction, in addition to high resolution transmission electron microscopy, are employed to analyse the crystal structure. The range and effects on properties of doping with the lower valence Ti cation on the Nb site (so-called acceptor doping) are examined. Electrical characterisation focuses on both high-temperature transport and the low-temperature, microwave-dielectric properties, highlighting the role of acceptor centres on the electrical behaviour.

## 2. Experimental

$Sr_3NdNb_3O_{12}$ (SNN) and Ti-doped phases $Sr_3NdNb_{3-x}Ti_xO_{12-\delta}$ ($0 \leq x \leq 0.1$) were prepared by solid-state reaction from dried precursors of $SrCO_3$, $Nd_2O_3$ $Nb_2O_5$ and $TiO_2$ (all Sigma Aldrich, 99.9% purity or higher) in the appropriate stoichiometric ratios. The reagents were firstly milled in acetone in an agate mortar, dried, and calcined at 1100 °C for 12 hours. Mixtures were subsequently fired at 1250 °C for 24 hours with intermediate grinding in an agate mortar, then attrition milled in isopropanol in teflon vials with $ZrO_2$ balls, dried and sieved. Pellets were uniaxially pressed from this powder and fired in the range 1300–1500 °C in air for up to 12 hours.

Completeness of reaction and phase purity were confirmed by powder X-ray diffraction (XRD) with a Bruker D8 diffractometer equipped with a solid-state rapid LynxEye detector, using monochromatic Cu K$\alpha_1$ radiation obtained with a Ge monochromator. The microstructure of polished surfaces, thermally etched at 1450 °C, were analysed by scanning electron microscopy (SEM) with a Zeiss DSM400 instrument.

For Rietveld refinement of the crystal structure, neutron-diffraction data were collected on the high-resolution powder diffractometer SPODI [17]

(Forschungsneutronenquelle Heinz-Maier Leibnitz (FRM II), Garching, Munich, Germany) over the scattering angle range $3 \leq 2\theta \leq 154°$. A wavelength of $\lambda = 1.5484$ Å was selected using a Ge (551) monochromator. Structural models were refined with the Fullprof software package [18].

The density of ceramics sintered at 1400 °C or greater was measured by the Archimedes method on displacement of water and was > 94% of the theoretical value. Porous pellets were also prepared for the purpose of measuring the $pO_2$ dependence of electrical conductivity at 900 °C, and for temperature-dependence conductivity measurements in reducing conditions where stabilisation with the atmosphere was found to be sluggish. For these samples, a porosity correction was made based on Archie's law [19,20]:

$$\sigma_B^{app} = \sigma_B^{\circ}(1 - P)^m \qquad (1)$$

where $\sigma_{\mathrm{B}}^{\mathrm{app}}$ is the apparent bulk conductivity, $\sigma_{\mathrm{B}}^{\circ}$ is the intrinsic bulk conductivity, P is the porosity of the sample and m is a constant based on geometric considerations (m ~ 2).

Samples for high-resolution transmission electron microscopy (HRTEM) were ground in n-butyl alcohol and ultrasonically dispersed. A few drops of the resulting suspension were deposited on a carbon-coated grid. Selected-area electron diffraction (SAED) and HRTEM were performed with a Jeol 300 FEG transmission electron microscope working at 300 kV.

For electrical-conductivity measurements, the pellets were lightly polished with SiC paper then coated with Au paste and fired at 950°C for 1 hour in air to remove the organic content, harden the Au and attach it to the pellet faces. Microwave dielectric measurements were performed on pellets sintered at 1500 °C for 6 h (x = 0) or 12 h (x = 0.06) with a relative density of ~ 98%.

High-temperature electrical-conductivity measurements were carried out with an Autolab PGStat302N impedance spectrometer employed in potentiostatic mode with a signal amplitude of 300 mV over the frequency range $1 \leq f \leq 10^6$ Hz. The temperature dependence of conductivity was determined from data collected on cooling in steps of 50 or 100 °C in the temperature range 550 – 800 °C in wet and dry air atmospheres. Dry gases were fed from the bottle through a drying column containing a commercial moisture trap of aluminosilicate- and zeolite-based beads. For wet atmospheres, gases were firstly bubbled through $H_2O$ or $D_2O$ (Apollon Scientific, 99.9%) at room temperature to provide a water content of ~ 0.03 atm [21].

The $pO_2$ dependence of conductivity in the range $6.5 \times 10^{-3} \lesssim pO_2 \lesssim 1$ atm was measured by impedance spectroscopy on mixing different ratios of dried flows of $O_2$ and $N_2$ via electronic mass-flow controllers (Bronkhorst); the actual $pO_2$ was monitored with an yttrium-stabilised zirconia sensor situated adjacent to the sample, and attached to an external voltmeter with Pt electrodes. Similarly, the $pH_2O$ dependence of conductivity in the range $10^{-3} \lesssim pH_2O \lesssim 10^{-1.5}$ atm was measured on mixing different ratios of dry and wet flows of air via the mass-flow controllers. To measure the $pO_2$ dependence of conductivity in reducing conditions, isothermal impedance measurements on porous pellets of $x = 0$ and 0.06 were collected as a function of $pO_2$ in a similar manner to that reported previously [8,22]; this method was adopted since mixing of hydrogen with a diluting gas (e.g. $N_2$) does not provide ready accessibility to incremental changes in $pO_2$ in the reducing range. The porous pellets were employed to enhance the equilibration times with the gas ambient. The cell was firstly equilibrated in dry 10% $H_2$:90% $N_2$ over a period of 2 days until the sample resistance had stabilised; the gas flow was then switched off and the chamber allowed to equilibrate over several days with the outside air. The $pO_2$ was measured in intervals of 20 minutes or longer with the yttrium-stabilised zirconia sensor. Analysis of impedance spectra was performed with the Zview 2.9c software (Scribner Associates) by fitting the data to appropriate equivalent circuits to resolve the response into bulk, grain-boundary and electrode contributions.

The MW dielectric properties were measured with an HP8510 Vector Network Analyser. $\varepsilon_r$ at MW frequencies was determined by the resonant-post method. The dielectric loss, Q, of the samples was measured using a transmission resonant cavity technique with an Au-coated brass cavity and fuse silica support employing a resonance frequency of ~ 6GHz. The temperature coefficient of resonance frequency ($\tau_f$) was registered for five temperatures in the range 25-84 °C.

## 3. Results and Discussion

### 3.1 Phase Analysis and Solid-solution Formation

The X-ray powder pattern of SNN sintered at 1500 °C for 6 hours showed the formation of a single phase which could be indexed by analogy with $Sr_3LaNb_3O_{12}$ on a hexagonal unit cell in space groups $R\overline{3}$ or $R\overline{3}m$. The synthesis of $Sr_3NdNb_3O_{12}$ has previously been described by Averkova et al. [23] who documented the formation of the series $Sr_3LnNb_3O_{12}$ (Ln = La – Nd); however, to date no structural characterisation of the Nd member has been reported. No secondary phases were identified in the XRD powder pattern or corresponding scanning electron micrographs.

The introduction of defects in metal oxides via substitution with aliovalent cations is widely exploited to induce functionality, including desirable electrical properties. The charge-compensation mechanism on substitution with a lower-valence cation involves the formation of one or more type of positively charged defect, commonly including mixed-cation valence states, oxide-ion vacancies, or protons when the vacancies become hydrated. As mentioned earlier, we recently reported proton transport in $Sr_3LaNb_3O_{12}$ for nominally stoichiometric and acceptor-doped phases [8]. In the present work, solid-solution formation on substituting Nb with Ti according to the series $Sr_3NdNb_{3-x}Ti_xO_{12-\delta}$ was examined. Single-phase material was obtained for x = 0.06 by XRD on final firing at 1500 °C for 12 hours, whereas experimentation with shorter firing times (6 h) or higher Ti contents ($x \geq 0.1$) resulted in the presence of second phases. Hence, the composition $Sr_3NdNb_{2.94}Ti_{0.06}O_{12-\delta}$ is expected to be close to the solid-solution limit for Ti doping on the Nb site.

Scanning electron micrographs of a thermally etched surface of $Sr_3NdNb_{2.94}Ti_{0.06}O_{12-\delta}$ are shown in Fig. 1 at two magnifications; no secondary phases were observed in accordance with the XRD phase analysis. The microstructure is composed of tightly packed platelets with a typical width of several microns and a thickness of the order of a micron; the platelets are generally much more elongated than those found in $Sr_3LaNb_3O_{12}$ [8]. The absence of cracks and open porosity are apparent in the micrographs. Similar micrographs, revealing a dense, microstructure of platelet-shaped grains, were obtained for Ti-doped and undoped samples, independent of the final atmospheric treatment.

## 3.2 Crystal Structure

As is widely known, tilting of the $BO_6$ octahedra of perovskite oxides involving slight movements of the oxygen positions may lead to a lowering of the space-group symmetry which is difficult to detect by X-ray diffraction due to the low X-ray scattering length of oxygen [24]. The oxygen sublattice is a much stronger scatterer of neutrons and electrons; however, whereas weak superlattice phenomena may still be difficult to observe by neutrons, electron diffraction is more sensitive to weak short-range reflections [25]. Consequently, SAED was employed to investigate the space group, accompanied by examination of the defect structure via collection of images by HRTEM. The space group of SNN was verified as $R\bar{3}$ or $R\bar{3}m$ by SAED. High-resolution transmission electron microscopy images projected along the [0 1 0] and [0 0 1] zone axes are shown in Fig. 2. The corresponding Fourier transform images along both zone axes, provided as insets, show a well-ordered material of rhombohedral symmetry with d-spacings of 4.9 and 27.1 Å, corresponding to $d_{100}$ and $d_{001}$ respectively. Contrast variation of the [010] zone axis image clearly shows the atomic positions: bright dots correspond to rows of Sr/Nd and Nb atoms, as superimposed in Fig. 2(a). No ordering between Sr and Nd was observed. An image calculation was performed employing the refined atomic parameters of SNN (see next section). The simulated image (inset in Figure 2(a)) provides a good fit to the experimental image at $\Delta t = 30$ Å and $\Delta f = -350$ Å.

Neutron powder diffraction (NPD) was undertaken to perform a more detailed structural refinement, not only for the much higher sensitivity to subtle oxygen movements in comparison to X-ray diffraction but also because the platelet-shaped grains of the SNN and Ti-doped SNN compositions resulted in excessive preferred orientation for in-house XRD patterns which proved difficult to model successfully. Analogous to the La-containing analogue, refinement of the NPD data of SNN was performed more successfully in space group $R\bar{3}$ ($R_{wp}$ = 5.05%) rather than in $R\bar{3}m$ ($R_{wp}$ = 22.8%) , the difference in the space groups residing in the allowance for octahedral tilting in the former. A non-assigned small peak was observed in the NPD pattern at 38.6 °2θ for the x = 0.06 sample, and corresponds to metallic Nb from the experimental setup. Structural parameters for the $Sr_3NdNb_{3-x}Ti_xO_{12-\delta}$ end members and agreement factors on refinement of NPD data are listed in Table 1. The observed NPD pattern of SNN and the difference pattern between observed and calculated data are shown in Fig. 3.

The refinements indicate occupation of the A1 site by Nd and Sr in approximately equivalent amounts and full occupation of the A2 site by Sr. In contrast to the case of $Sr_3LaNb_3O_{12}$ [8], there was no evidence for the presence of a slightly higher Sr content on the A1 site which could explain the acceptor-dopant behaviour of the nominally undoped phase (discussed in section 3.3). Nevertheless, Sr and Nd have comparable neutron scattering lengths and the minor quantities of acceptor dopant required to control the defect concentrations and thereby influence the electrical properties may be difficult to determine employing diffraction methods. The Ti-doped sample attained the lowest refinement parameters on location of Ti on the Nb(2) site and the oxygen vacancies on the O(1) site.

A schematic diagram of the ion arrangement in $Sr_3NdNb_3O_{12}$ is shown in Fig. 4(a). The structure consists of the stacking of four $(hhcc)_3$ sequences of $AO_3$ close-packed layers along the c axis of the unit cell. Nb(1) and Nb(2) ions are located between ccp and hcp layers and between two ccp layers, respectively, whereas the cation sites between adjacent hcp layers are vacant. This gives rise to blocks of three-layer-thick, corner-sharing octahedra ($Nb(1)O_6$-$Nb(2)O_6$-$Nb(1)O_6$) with B-cation vacancies occurring every fourth layer. Successive octahedral blocks are shifted by a ⅓ $\langle 01\bar{1}0\rangle_H$ vector (“shift”-type structure [26]). The $Nb(2)O_6$ octahedra in the centre of the layers are perfectly regular and undistorted; however, the Nb(1) ions are displaced along the c axis towards the adjacent cation vacancies, giving rise to highly distorted $Nb(1)O_6$ octahedra, as shown in Fig. 4(b); selected bond lengths, octahedral distortions and additional structural information are provided in Table 2. The mixed Nd/Sr(1)-occupied sites are situated within the layers of corner-sharing octahedral blocks, and the Sr(2) sites are located adjacent to the B-site vacancies.

In space group $R\bar{3}$, the octahedra of the three-layer blocks are tilted along the Cartesian x, y and z axes of the pseudocubic subcell according to the $a^-a^-a^-$ tilt system (Glazer notation[27]). That is, there are three anti-phase tilts of equal magnitude around the pseudo-cubic directions, as illustrated schematically in Fig. 4(c) for a fragment of the three-layer-thick block projected down the c axis of the unit cell. The octahedral tilts, listed in Table 2, were estimated from the N(1)-O(1)-Nb(2) bond angle (ω), obtained from the neutron data as (180 – ω)/2.

## 3.3 High-temperature Electrical Characterisation

Complex impedance, Z* plots of $Sr_3NdNb_{3-x}Ti_xO_{12-\delta}$ (x = 0, 0.06) in oxidising conditions at high temperature (550–800°C) were dominated by a large, slightly depressed, high-frequency arc accompanied by a poorly resolved low-frequency response, Fig. 5. The large arc was modelled by a single RQ element with an estimated capacitance of $C = Q^{1/n}R^{1-n/n}$. A value of 4.6 pFcm$^{-1}$ was calculated at 700 °C in air, typical of a bulk contribution for samples with $\varepsilon_r$ ~10$^{1\text{-}2}$ [28]. As is the case for the La-containing analogue [8], there is clear evidence of proton transport from the impedance spectra, as indicated by both the higher conductivity in wet in comparison to dry conditions and the observance of a conductive isotope effect; the conductivity in air moistened with $H_2O$ at 700 °C is a factor of 1.15 greater than that measured in $D_2O$-wetted air.

The temperature dependence of the bulk electrical conductivity for $Sr_3NdNb_{3-x}Ti_xO_{12-\delta}$ (x = 0, 0.06) in dry air and air humidified with $H_2O$ and $D_2O$ is shown in Fig. 6; data for $Sr_3LaNb_3O_{12}$ and $Sr_3LaNb_{2.9}Ti_{0.1}O_{12-\delta}$ in wet air taken from ref. 8 are also plotted for comparison. Both the conductivity in wet air and the difference in conductivity between wet and dry regimes for SNN increase significantly on Ti doping. The introduction of the lower-valence Ti dopant directly increases proton transport through the hydration of oxygen vacancies and the creation of mobile protons in accordance with the equilibrium

$$H_2O + V_o^{\cdot\cdot} + O_o^{\times} \Leftrightarrow 2OH^{\cdot} \qquad (2)$$

where the mass-action law relates the concentration of the species by means of the corresponding equilibrium constant $K_W$ according to

$$K_W[V_o^{\cdot\cdot}]pH_2O = [OH_o^{\cdot}]^2 \qquad (3)$$

The inset of Fig. 6 shows the greater magnitude of the isotope effect in moistened air for the Ti-doped as compared to the undoped sample, resulting from a greater contribution of protonic carriers to transport in the Ti-containing material. The effect of increasing temperature is to diminish the conductive isotope effect as a result of the exothermic nature of the above equilibrium, which results in a lower proton content and a higher concentration of competing charge carriers (discussed below). A further manifestation of this is the smooth transition to a slightly higher activation-energy, $E_a$, regime with increasing temperature in the Arrhenius plots; this behaviour is fairly typical of oxide proton conductors [29].

The activation energies in wet and dry oxidising conditions, listed in Fig. 6, were calculated in the temperature range 550–700 °C where proton transport is expected to dominate and before any discernible inflection to a higher activation-energy regime takes place. Both end-members of the $Sr_3NdNb_{3-x}Ti_xO_{12-\delta}$ series exhibited slightly greater $E_a$ values in $D_2O$-containing air, 0.84 and 0.92 eV for $x = 0$ and 0.06, respectively, in comparison to wet air, the difference ($\Delta \sim 0.03–0.07$) being approximate to that expected between proton and deuteron hopping [3]. The activation energies in wet oxidising conditions for the Nd-containing series are somewhat lower than those observed in $Sr_3LaNb_3O_{12}$ (0.93-1.13eV, ref 8); however, the effect of adding Ti dopant to the Nd series is not to lower the $E_a$ for proton conduction with respect to the undoped phase, as was observed on doping $Sr_3LaNb_3O_{12}$. It is notable that conductivity is higher in wet oxidising conditions for the Ti-doped, Nd-containing phase ($x = 0.06$) in comparison to the La-containing analogue with $x = 0.1$, despite a lower acceptor dopant level. The reasons for this are not readily apparent. One possible explanation could be that proton hopping distances to neighbouring oxygen sites are slightly shorter due to the smaller ionic radius of Nd resulting in a smaller $Sr_3NdNb_3O_{12}$ unit cell compared to the larger La ion in $Sr_3LaNd_3O_{12}$.

The electrical-conductivity dependencies of selected partial-pressure variations of the $Sr_3NdNb_{3-x}Ti_xO_{12-\delta}$ system are shown in Fig. 7. In dry oxidising conditions, Fig. 7(a), the positive conductivity dependence on $pO_2$ at 800 °C is suggestive of a p-type contribution to transport. Under these conditions, oxidation is expected to occur according to (Kröger-Vink notation)

$$V_O^{\cdot\cdot} + {}^{1}\!/_{2}\, O_2 \rightleftharpoons O_o^{\times} + 2h^{\cdot} \quad (4)$$

giving the mass-action expression

$$p^2 = K_o[V_O^{\cdot\cdot}]pO_2^{1/2} \quad (5)$$

where $K_o$ is the mass-action constant for the oxidation reaction. Assuming that the oxygen vacancies are the major positive carriers, the charge-neutrality condition in this region is

$$[A'] = 2[V_o^{\cdot\cdot}] \quad (6)$$

and combining with eq. (5) gives the number of electron-hole charge carriers and conductivity as proportional to $pO_2^{+1/4}$ [30,31]. The value of the exponent at 800 °C ($\sigma \propto pO_2^{0.14}$) thus indicates a significant contribution from electron holes to transport. In contrast, the $pO_2$ dependence of conductivity is close to zero at 600 °C, suggesting the conductivity is dominated by oxide-ion charge carriers at this temperature, the concentration of which is effectively independent of $pO_2$. The exponent of 0.14 at 800 °C, lying between the values expected for pure p-type and pure oxide-ion conductivity, is, therefore, reflective of mixed p-type and oxide-ion transport. The higher activation-energy regime in the Arrhenius plots, which evolves with increasing temperature in wet conditions, Fig. 6, can thus be understood to result from an increasing contribution of both oxide-ion and p-type charge carriers on the exothermic loss of protonic charge carriers.

In conditions of low $pO_2$, the equilibrium loss of oxygen is expressed by the reduction reaction

$$O_o^{\times} \Leftrightarrow {}^{1}\!/_{2}\, O_2 + V_o^{\cdot\cdot} + 2e' \quad (7)$$

and corresponding mass-action expression

$$[V_o^{\cdot\cdot}]n^2 = K_r pO_2^{-1/2} \quad (8)$$

where $K_r$ is the mass-action constant. It follows that the number of electron charge carriers n and thereby conductivity is proportional to $pO_2^{-1/6}$ when reduction is the major source of defects (intrinsic model, refs. 30,32) and charge neutrality is approximated by

$$n \approx 2[V_o^{\cdot\cdot}] \quad (9)$$

In less extreme reducing conditions, the charge-neutrality condition is represented by eq. (6) which, on substituting into the mass-action expression (eq. (8)), shows that n is proportional to $pO_2^{-1/4}$, according to the extrinsic model for defect formation [30–32]. The $pO_2$ dependencies of conductivity of SNN and Ti-doped SNN in reducing conditions, Fig. 7 (b), are thus n-type, as revealed by a negative power-law relationship with a gradient close to the theoretical value for pure n-type transport of –¼ in the range $10^{-8} \lesssim pO_2 \lesssim 10^{-23}$ atm at 900 °C. The isothermal measurement was performed at this temperature to limit any possible influence of protons on the determined dependency. The change in slope, closer to a -1/6 dependence, occurring below this range, ($< 10^{-23}$ atm) is likely to result from intrinsic defect formation whereupon the reduction reaction (eq.(7)) is the major source of defects.

The behaviour presented by SNN in reducing conditions is consistent with that of both nominally undoped $BaTiO_3$ and $Sr_3LaNb_3O_{12}$ [8,30]. The –¼ power-law dependence of the former phase has been attributed to small amounts of acceptor impurity A′ on the perovskite B site. Equally, we speculated in our earlier work on the hexagonal perovksite $Sr_3LaNb_3O_{12}$ [8] that “self doping” of the La/Sr A1 site with a slight excess of Sr would also result in the generation of positive oxygen-vacancy defects. In the case of the La-containing analogue, it was argued that such off-stoichiometric behaviour results in excess La which may be present as surface $La(OH_3)$.

In wet oxidising conditions, in the temperature range encompassed by the low-activation-energy regime below 700 °C (Fig. 6), the defect concentration is principally dependent on the hydration reaction eq. (2), whereby the acceptor centres are charge compensated by protons and oxygen vacancies:

$$[A'] = 2[V_O^{\cdot\cdot}] + [OH_O^{\cdot}] \qquad (10)$$

Assuming the above electroneutrality condition, when acceptor dopants are charge compensated principally by oxygen vacancies ($[V_O^{\cdot\cdot}] \gg [OH_O^{\cdot}]$) protons as a minority defect exhibit a concentration dependence of $p(H_2O)^{1/2}$ [29]; on the other hand, if protons are the majority charge-compensating defect ($[V_O^{\cdot\cdot}] \ll [OH_O^{\cdot}]$), proton conductivity is independent of the water-vapour partial pressure ($\sigma \propto p(H_2O)^0$). The protonic conductivity dependency with $\sigma \propto p(H_2O)^{0.20}$ at 800 °C for SNN, Fig. 7 (c), lies between these two limiting defect situations. We note that although this dependency is a further indication of proton transport in wet oxidising conditions, the component is likely to be partially influenced by the presence of competing positive charge carriers (oxide ions and electron holes) as analysed below.

### 3.4. Numerical analysis of defect equilibria

The experimental conductivity results were further examined employing solution of the expected defect equilibria. Under wet oxidising conditions, the concentration of different species is governed by simultaneous equilibria of equations (2) and (4), with the general electroneutrality condition expressed as

$$[A'] \approx [OH_O^{\cdot}] + 2[V_O^{\cdot\cdot}] + p \qquad (11)$$

Recombination of eqs. (3), (5) and (11) provides a relation between the concentration of all the species in a unique polynomial equation according to

$$2y^2 + (M + N)y - [A'] = 0 \qquad (12)$$

where

$$y = [V_O^{\cdot\cdot}]^{1/2} \qquad (13)$$

$$p = K_h^{1/2} pO_2^{1/4} [V_O^{\cdot\cdot}]^{1/2} = M\,y \qquad (14)$$

and

$$p = K_w^{1/2} pH_2O^{1/2} [V_O^{\cdot\cdot}]^{1/2} = N\,y \qquad (15)$$

The solution of Eq. (12) for various values of $pH_2O$ gives the defect profiles for each species according to Eqs. (13)-(15). We note that the approximation used in the analysis considers that $[O_O^X]$ is constant and that the concentration of n-type carriers is negligible under the studied oxidising conditions. The estimation of the concentration of the various defects was performed by assuming values of equilibrium constants for Eqs. (3) and (5) consistent with those previously reported for perovskite-based protonic conductors [33–35]; Table 3(a) lists the equilibrium constants employed in the current fitting compared to previously employed values for similar systems. After obtaining the defect profiles, the conductivity of the various transport species as a function of $pH_2O$ was simulated by assuming relations between the mobility of carriers similar to those reported in the literature [34] (Table 3(b)). The mobilities were slightly modified in order to obtain a suitable fitting of total conductivity with the experimental results as a function of both $pH_2O$ and $pO_2$ in dry conditions.

The simulated conductivity associated to the different carriers, fitted according to the criteria mentioned above, and comparison with the experimental results of total conductivity are shown in Figs. 8 and 9 for x = 0 and x = 0.06, respectively. The simulated conductivities of the different species as interpreted by the defect chemistry, although only representing estimations of the transport behaviour, fit the experimental data very well. The fitting results indicate that the total conductivity under wet conditions is mainly governed by protons in wetter atmospheres; however, their contribution to transport decreases drastically as $pH_2O$ decreases, with concomitant increases in contributions from oxide ions and electronic carriers. Considering that the presence of protonic defects requires the existence of oxygen vacancies in the dry state, which are hydrated on exposure to wet atmospheres according to Eq. (2), the simulated results corresponding to x = 0 were obtained with an acceptor-centre content of 0.013. These acceptor centres, a requirement for the charge-compensation of positive defects (Eq. 11), are indicated to be present by the $pO_2$ power-law dependencies of conductivity (Fig. 7). As mentioned previously, the presence of acceptor centres in the undoped phase may arise from unavoidable acceptor impurities or self-doping of Sr on the Nd site.

### 3.5 Microwave-dielectric measurements

The microwave-dielectric properties of $Sr_3NdNb_{3-x}Ti_xO_{12}$ (x = 0 and 0.06) are listed in Table 4. The relative permittivity, $\varepsilon_r$ ~ 37–39, is only marginally higher than that of $Sr_3LaNb_3O_{12}$ ($\varepsilon_r$ ~ 36) [14], which is to be expected based on the similar polarisability of the constituent cations [36,37]. The Q × f value of the title phase is, however, somewhat lower than the varied values measured for SLN (23,500 GHz, ref. 14; 45,327 GHz ref 15). The effect of Ti doping on SNN is to introduce additional dielectric loss, probably attributable to the much greater concentration of point defects (principally oxygen vacancies). Neither of the Nd-containing materials offer a Q × f value that could be considered competitive with commercial high-performance dielectric materials with $\varepsilon_r$ ~ 35 -40. The presence of acceptor centres in both the title phase and $Sr_3LaNb_3O_{12}$, which has been seen to heavily influence the high-temperature electrical behaviour via the electroneutrality condition represented by eq. (6), are likely to contribute to the dielectric loss. Hence, sample processing may have a significant influence on the measured Q × f value [38]. Indeed, this appears to be the case for the La-containing analogue, as expounded by the divergence of the values quoted in different studies. Moreover, texturing of the platelet structure of these materials may have a dramatic impact on limiting the dielectric loss [39].

The $\tau_f$ value is low for both samples but is also sensitive to the dopant content, lowering to only -3 ppm / °C for the sample x = 0.06 (Table 4). Whereas $\tau_f$ in many 3C-type $ABO_3$ perovskites is influenced by the tolerance factor and the tilt system of the $BO_6$ octahedra [11], the structure–property relations in hexagonal perovskites are less well understood. However, Sinclair and co-workers [14] have shown that a lower tolerance factor and larger tilt angle in $Sr_3LaNb_3O_{12}$ compared to $Ba_3LaNb_3O_{12}$ (BLN) increases the transition temperature to an untilted system ($T_{tilt}$) thereby lowering both $\varepsilon_r$ and the gradient of $\varepsilon_r$ versus temperature, correlated with a lowering of the magnitude of $\tau_f$ from -100 (BLN) to -5 ppm/°C (SLN). Here, the effect of lowering the tolerance factor (Table 2) in the Nd-containing analogues also appears to lower $\tau_f$ considerably in comparison to BLN, whereas the much slighter differences in $\tau_f$ between SLN and the Nd-containing phases do not directly correlate with tolerance factor and may be attributable to additional factors such as processing conditions.

## 4. Conclusions

The observance of moderate levels of proton conductivity in $Sr_3NdNb_3O_{12}$ is the second such example in a 12R-type hexagonal pervoskite and suggests the presence of protonic defects in this structure type and related hexagonal perovskites may be quite widespread. The protons are introduced in the nominally undoped phase by acceptor centres arising from unavoidable acceptor impurities or over stoichiometry of Sr on the A1 site. These acceptor centres also control the defect behaviour in reducing conditions, as revealed by a power-law dependence on $pO_2$ of -¼ in the range $10^{-19} \lesssim pO_2 \lesssim 10^{-8}$ atm in accordance with defect formation via the intrinsic model. In dry, oxidising conditions, the conductivity is principally via oxide-ion vacancies at 600 °C with p-type charge carriers contributing to transport at higher temperature. On introducing significant quantities of acceptor dopant via the solid solution $Sr_3Nb_{3-x}Ti_xO_{12-\delta}$ ($0 \leq x \leq$

0.06), conductivity increases substantially, whether via protons (wet oxidising conditions) or oxide-ions and p-type charge carriers (dry oxidising conditions).

$Sr_3NdNb_3O_{12}$ exhibits a moderately high permittivity, $\varepsilon \sim 37$, a quality factor $Q \times f \sim 16400$ GHz (at 6.3 GHz) and low coefficient of resonant frequency, $\tau_f \sim 12$ppm /°C. The effects of acceptor doping with Ti on the Nb site are to lower the quality factor to ~13600 and $\tau_f$ to near-zero ($\tau_f \sim 3$ppm /°C). The higher dielectric loss in the Ti-doped phase most probably results from a much higher concentration of point defects. Dielectric loss in the undoped phase may be improved by changes in the processing which limits the role of acceptor impurities and optimises the highly oriented platelet-like microstructure.

## Acknowledgements

We thank CAPES (Brazil, project no. BEX 9119/11-6), MINECO (Spain, ENE2012-30929) and CSIC (Spain, i-link0743) for funding.

Table1. Structural parameters for $Sr_3NdNb_{3-x}Ti_xO_{12-\delta}$ obtained from NPD data

| | **$Sr_3NdNb_3O_{12}$[a]** | **$Sr_3NdNb_{2.94}Ti_{0.06}O_{12-\delta}$[b]** |
|---|---|---|
| **$a_h$ (Å)** | 5.64213(3) | 5.63855(6) |
| **$c_h$ (Å)** | 27.1506(2) | 27.1452(4) |
| **Sr(1)/Nd(1) position 6c** | | |
| **Occ Sr/Nd** | 0.5/0.5 | 0.5/0.5 |
| **z** | 0.28499(9) | 0.2845(1) |
| **U*100 (Å$^2$)** | 0.80(4) | 0.93(9) |
| **Sr(2) position 6c** | | |
| **z** | 0.1391(1) | 0.1386(2) |
| **Occ** | 1.0 | 1.0 |
| **U*100 (Å$^2$)** | 1.09(6) | 1.4(1) |
| **Nb(1) position 6c** | | |
| **z** | 0.42378(8) | 0.4241(1) |
| **Occ** | 1.0 | 1.0 |
| **U*100 (Å$^2$)** | 0.22(2) | 0.32(5) |
| **Nb(2)/Ti(1) position** | | |
| **Occ** | 1.0/0.0 | 0.94/0.06 |
| **U*100 (Å$^2$)** | 0.22(2) | 0.32(5) |
| **O(1) position 18f** | | |
| **x** | 0.2174(5) | 0.2164(8) |
| **y** | 0.8909(4) | 0.8889(7) |
| **z** | 0.62750(7) | 0.6274(1) |
| **Occ** | 1.0 | 0.9183 |
| **U*100 (Å$^2$)** | 1.48(3) | 1.24(6) |
| **O(2) position 9d** | | |
| **x** | 0.2284(2) | 0.2290(5) |
| **y** | 0.8933(4) | 0.8928(6) |
| **z** | 0.45367(6) | 0.4542(1) |
| **Occ** | 1.0 | 1.0 |
| **U*100 (Å$^2$)** | 1.14(3) | 1.38(6) |

Space Group $R\bar{3}$ (#148, hexagonal setting): 3a (0 0 0), 6c (0 0 z), 18f (x y z)

[a] $\chi^2$= 4.00 , $R_{wp}$= 5.05%, $R_{exp}$= 2.48%, $R_B$= 4.45%, $\rho_{(cryst)}$ = 5.842 g/cm$^3$

[b] $\chi^2$= 9.27, $R_{wp}$= 7.80%, $R_{exp}$= 2.56%, $R_B$= 4.91%, $\rho_{(cryst)}$ = 5.781 g/cm$^3$

Table 2. Selected structural information for $Sr_3NdNb_{3-x}Ti_xO_{12-\delta}$ obtained from NPD data. Angles are given in degrees and distances in Å, distortion Δ of the $BO_n$ polyhedra and perovskite tolerance factor, t, are also reported. $\Delta = 1/n\ \Sigma_{j=1,n}\ \{(d_n - \langle d(B\text{-}O)\rangle) / \langle d(B\text{-}O)\rangle\}^2$ and $t = \langle r(A)\rangle + r(O) / \sqrt{2}\ \langle r(B)\rangle + r(O)$; where r(A), r(B) and r(O) are the A, B and O average ionic radii, respectively [40].

| | $Sr_3NdNb_3O_{12}$ | $Sr_3NdNb_{2.94}Ti_{0.06}O_{12-\delta}$ |
|---|---|---|
| **[a]tilt angle ω (deg)** | 9.50 | 9.25 |
| **Nb(1)-O(1) (Å)** | 2.139(3) | 2.144(5) |
| | 2.139(3) × 2 | 2.144(4) × 2 |
| **Nb(1)-O(2) (Å)** | 1.859(2) × 3 | 1.866(4) × 2 |
| | | 1.866(3) |
| **average Nb(1)-O (Å)** | 1.999(1) | 2.005(2) |
| **distortion $Nb(1)O_6$ $\times 10^{-4}$** | 49.015 | 48.212 |
| **Nb(2)/Ti(1)-O(1) (Å)** | 1.997(2) × 4 | 1.992(3) × 2 |
| | 1.997(3) × 2 | 1.992(4) × 2 |
| | | 1.992(5) × 2 |
| **average Nb(2)/Ti(1)-O (Å)** | 1.997(1) | 1.992(2) |
| **distortion $Nb(2)/Ti(1)O_6$ $\times 10^{-4}$** | 0.001 | 0.0 |
| **average Sr(1)-O (Å)** | 2.776(3) | 2.778(4) |
| **average Sr(2)-O (Å)** | 2.883(2) | 2.874(4) |
| **unit-cell volume ($Å^3$)** | 748.509(7) | 747.41(2) |
| **tolerance factor** | 0.970 | 0.968 |

[a] along [100] of the pseudocubic cell

Table 3.

(a) Equilibrium constants employed for the simulation of defect profiles as function of $pH_2O$. Data from literature are shown for comparison.

| Phase | Equilibrium constants | Reference |
|---|---|---|
| $Sr_3NdNb_{2.94}Ti_{0.06}O_{12-\delta}$ | $K_W$= 30 atm$^{-1}$, $K_O$= 5x10$^{-6}$ atm$^{-1/2}$ | this work |
| $Sr_3NdNb_3O_{12-\delta}$ | $K_W$= 2 atm$^{-1}$, $K_O$= 10$^{-6}$ atm$^{-1/2}$ | this work |
| $A^{2+}B^{4+}_{0.9}M^{3+}_{0.1}O_{2.95\pm\delta}$ | $K_W$= 20 atm$^{-1}$, $K_O$= 10$^{-5}$ atm$^{-1/2}$ | 35 |
| $SrCe_{0.95}Yb_{0.05}O_{3-\delta}$ | $K_W$= 4.24x10$^{-6}$ exp(14214/T) atm$^{-1}$<br>$K_O$= 5x10$^{-6}$ atm$^{-1/2}$ | 34 |

(b) Mobility ratio between different charge carriers used for the simulation of conductivity behaviour as function of $pH_2O$ compared to data from literature.

| Phase | Mobility ratio | Reference |
|---|---|---|
| $Sr_3NdNb_{2.94}Ti_{0.06}O_{12-\delta}$ (800 °C) | $\mu_h/\mu_H = 63$; $\mu_V/\mu_H \sim 0.27$ | this work |
| $Sr_3NdNb_3O_{12-\delta}$ (800 °C) | $\mu_h/\mu_H = 60$; $\mu_V/\mu_H \sim 0.37$ | this work |
| $SrCe_{0.95}Yb_{0.05}O_{3-\delta}$ (900° C) | $\mu_h/\mu_H \sim 100$; $2\mu_V/\mu_H \sim 0.1$ | 34 |

Table 4.

Microwave-dielectric properties of $Sr_3NdNb_{3-x}Ti_xO_{12-\delta}$.

| Sample (x) | $f_o$ (GHz) | $Qf_0$ (GHz) | $\varepsilon_r$ | T*CF* ($\tau_f$) (ppm/°C) |
|---|---|---|---|---|
| 0 | 6.39 | 16422 | 37.0 | -12 |
| 0.06 | 6.23 | 13640 | 39.2 | -3 |

## Figure Captions

1. Scanning electron micrographs of $Sr_3NdNb_{2.94}Ti_{0.06}O_{12-\delta}$ at magnifications of (a) 600× and (b) 1800× showing platelet-like microstructure.

2. High-resolution transmission electron microscopy images of $Sr_3NdNb_3O_{12}$ projected down the (a) [0 1 0] and (b) [0 0 1] zone axes. The corresponding selected area electron diffraction patterns are shown as insets (bottom-right corners).

3. Observed (circles), calculated (continuous line) and difference (continuous line at bottom) neutron powder diffraction profiles of (a) $Sr_3NdNb_3O_{12}$ and (b) $Sr_3NdNb_{2.94}Ti_{0.06}O_{12-\delta}$. Vertical bars indicate the expected position of Bragg peaks. The presence of a Nb parasite peak arising from the experimental set-up is indicated in Fig. 3(b).

4. Schematic diagrams of the $Sr_3NdNb_3O_{12}$ structure: (a) projection down the [1 0 0] zone axis, showing hhcc stacking sequence of $AO_3$ layers; (b) represention of $Nb(1)O_6$ octahedron showing displacement of Nb towards a cation-site vacancy; (c) projection down the [0 0 1] zone axis showing octahedral tilting according to the $a^-a^-a^-$ tilt system along the pseudo-cubic cell directions.

5. Z* plots of $Sr_3NdNb_3O_{12}$ in dry and humidified air at 700 °C (numbers refer to the approximate value of $\log_{10}$ of the frequency in Hz).

6. Temperature dependencies of the bulk conductivity of the $Sr_3NdNb_{3-x}Ti_xO_{12-\delta}$ and $Sr_3LaNb_{3-x}Ti_xO_{12-\delta}$ (from ref. 8) in dry and wet air shown with open and shaded symbols, respectively. The inset shows the magnitude of the conductive isotope effect for x = 0 and 0.06 members of the Nd-containing series as a function of temperature employing conductivity data collected in $D_2O$-wetted air.

7. Selected partial-pressure dependencies of electrical conductivity for $Sr_3NdNb_{3-x}Ti_xO_{12-\delta}$ (x = 0 and 0.06): (a) bulk conductivity as a function of $pO_2$ in dry oxidising conditions; (b) total conductivity as a function of $pO_2$ in reducing conditions; (c) bulk conductivity as a function of $pH_2O$ in oxidising atmosphere.

8. Simulated conductivity of transport carriers and total conductivity at 800 °C as a function of $pH_2O$ (a) and $pO_2$ (b) and comparison with the experimental results of total conductivity (closed squares) for $Sr_3NdNb_3O_{12-\delta}$.

9. Simulated conductivity profiles of transport species and total conductivity at 800 °C as a function of (a) $pH_2O$ and (b) $pO_2$ showing fit with the experimental results of total conductivity (closed squares) for $Sr_3NdNb_{2.94}Ti_{0.06}O_{12-\delta}$.

## References

1 L. Katz and R. Ward, Inorg. Chem., 1964, **3**, 205–211.

2 J. Darriet and M. A. Subramanian, J. Mater. Chem., 1995, **5**, 543–552.

3 T. Norby, M. Widerøe, R. Glöckner and Y. Larring, Dalt. Trans., 2004, 3012–3018.

4 K. D. Kreuer, Annu. Rev. Mater. Res., 2003, **33**, 333–359.

5 E. Fabbri, D. Pergolesi and E. Traversa, Chem. Soc. Rev., 2010, **39**, 4355–69.

6 K. Kreuer, Solid State Ionics, 1997, **97**, 1–15.

7 R. Haugsrud and T. Norby, Nat. Mater., 2006, **5**, 193–196.

8 C. Tabacaru, A. Aguadero, J. Sanz, A. L. Chinelatto, A. Thursfield, D. Pérez-Coll, I. S. Metcalfe, M. T. Fernandez-Díaz and G. C. Mather, Solid State Ionics, 2013, **253**, 239–246.

9 A. Feteira, D. C. Sinclair, I. M. Reaney, Y. Somiya and M. T. Lanagan, 2004, **1087**, 1082–1087.

10 I. M. Reaney and D. Iddles, J. Am. Ceram. Soc., 2006, **89**, 2063–2072.

11 E. L. Colla, I. M. Reaney and N. Setter, J. Appl. Phys., 1993, **74**, 3414–3425.

12 H. Yamada, T. Okawa, Y. Tohdo and H. Ohsato, J. Eur. Ceram. Soc., 2006, **26**, 2059–2062.

13 G. M. Keith, C. A. Kirk, K. Sarma, N. M. Alford, E. J. Cussen, M. J. Rosseinsky and D. C. Sinclair, Chem. Mater., 2004, 2007–2015.

14 R. Rawal, A. J. McQueen, L. J. Gillie, N. C. Hyatt, E. E. McCabe, K. Samara, N. M. Alford, A. Feteira, I. M. Reaney and D. C. Sinclair, Appl. Phys. Lett., 2009, **94**, 192904.

15 L. Fang, H. Zhang, Q. Yu, H. Su, B. Wu and X. Cui, J. Am. Ceram. Soc., 2009, **92**, 556–558.

16 R. M. Adams, University of Huddersfield, 2010.

17 M. Hoelzel, a. Senyshyn, N. Juenke, H. Boysen, W. Schmahl and H. Fuess, Nucl. Instruments Methods Phys. Res. Sect. A Accel. Spectrometers, Detect. Assoc. Equip., 2012, **667**, 32–37.

18 J. Rodriguez-Carvajal, Phys. B, 1993, **192**, 55–69.

19 M. C. Steil, T. F. and M. Kleitz, J. Electrochem. Soc., 2000, **144**, 390–398.

20 D. Pérez-Coll, E. Sánchez-López and G. C. Mather, Solid State Ionics, 2010, **181**, 20–26.

21 L. Haar, J. S. Gallagher and G. S. Kell, NBS/NRC Steam Tables, Hemisphere Publishing Corporation, New York, 1984.

22 J. C. Pérez Flores, C. Ritter, D. Pérez-Coll, G. C. Mather, F. García-Alvarado and U. Amador, J. Mater. Chem., 2011, **21**, 13195–13204.

23 O. E. Averkova, E. A.A. and V. P. Sirotinkin, Russ. J. Inorg. Chem., 1987, **32**, 1183.

24 C. J. Howard, K. S. Knight, B. J. Kennedy and E. H. Kisi, J. Phys. Condens. Matter, 2000, **12**, L677–L683.

25 D. I. Woodward and I. M. Reaney, Acta Crystallogr. B., 2005, **61**, 387–99.

26 G. Trolliard, N. Ténèze, P. Boullay and D. Mercurio, J. Solid State Chem., 2004, **177**, 1188–1196.

27 A. M. Glazer, Acta Crystallogr. Sect. B Struct. Crystallogr. Cryst. Chem., 1972, **28**, 3384–3392.

28 J. T. S. Irvine, D. C. Sinclair and A. R. West, Adv. Mater., 1990, **2**, 132–138.

29 R. Haugsrud and T. Norby, Solid State Ionics, 2006, **177**, 1129–1135.

30 N. Chan, R. Sharma and D. Smyth, J. Am. Ceram. Soc., 1981, **64**, 556–562.

31 M. J. Rampling, G. C. Mather, F. M. B. Marques and D. C. Sinclair, J. Eur. Ceram. Soc., 2003, **23**, 1911–1917.

32 N.-H. Chan, R. K. Sharma and D. M. Smyth, J. Am. Ceram. Soc., 1982, **65**, 167–170.

33 F. Krug, T. Schober and T. Springer, Solid State Ionics, 1995, **81**, 111–118.

34 T. Schober, W. Schilling and H. Wenzl, Solid State Ionics, 1996, **86-88**, 653–658.

35 N. Bonanos and F. W. Poulsen, J. Mater. Chem., 1999, **9**, 431–434.

36 C. Vineis, P. K. Davies, T. Negas and S. Bell, Mater. Res. Bull., 1996, **31**, 431–437.

37 R. D. Shannon, J. Appl. Phys., 1993, **73**, 348–366.

38 M. Li, A. Feteira, M. Mirsaneh, S. Lee, M. T. Lanagan, C. a. Randall and D. C. Sinclair, J. Am. Ceram. Soc., 2010, **93**, 4087–4095.

39 K. Wada, Y. Fukami, K. Kakimoto and H. Ohsato, Jpn. J. Appl. Phys., 2005, **44**, 7094–7097.

40 R. D. Shannon, Acta Crystallogr. Sect. A, 1976, **32**, 751–767.

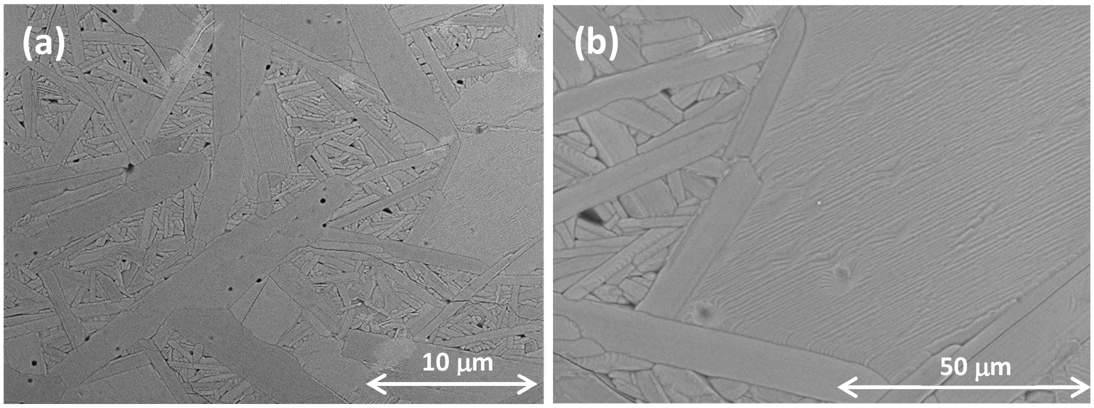

Fig. 1. Scanning electron micrographs of $Sr_3NdNb_{2.94}Ti_{0.06}O_{12-\delta}$ at magnifications of (a) 600× and (b) 1800× showing dense platelet-like microstructure.

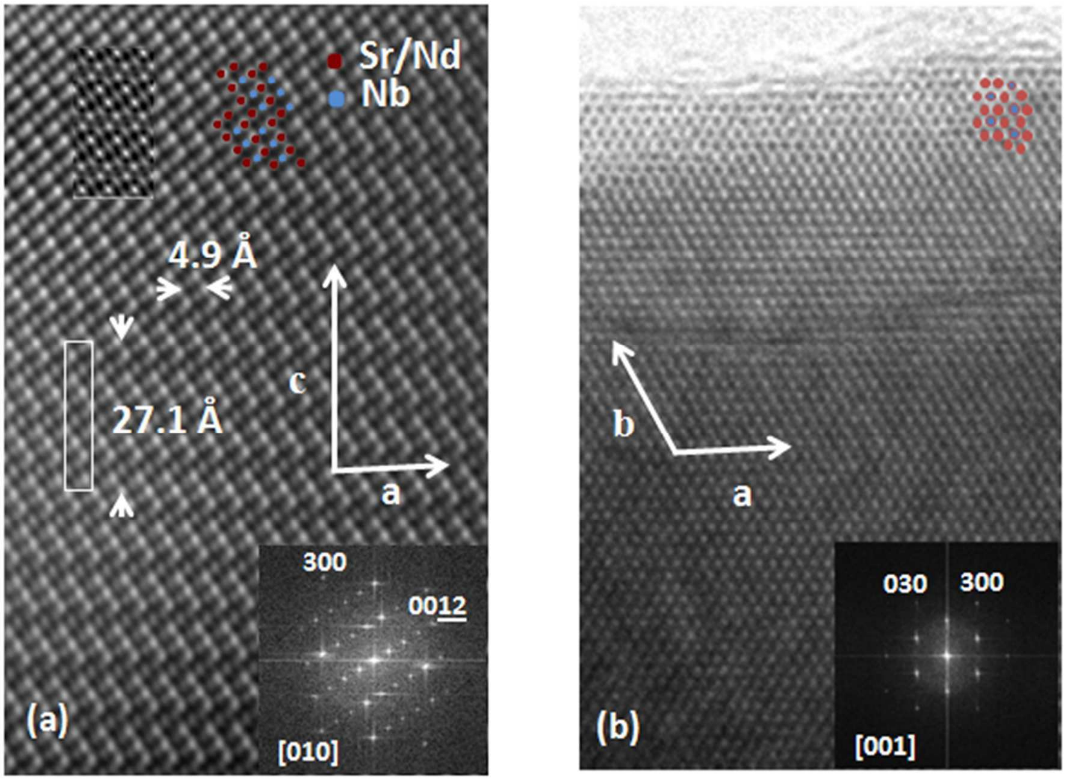

Fig. 2. High-resolution transmission electron microscopy images of $Sr_3NdNb_3O_{12}$ projected down the (a) [0 1 0] and (b) [0 0 1] zone axes. The corresponding Fourier transforms are shown as insets (bottom-right corners); a simulated image is also shown as inset in (a).

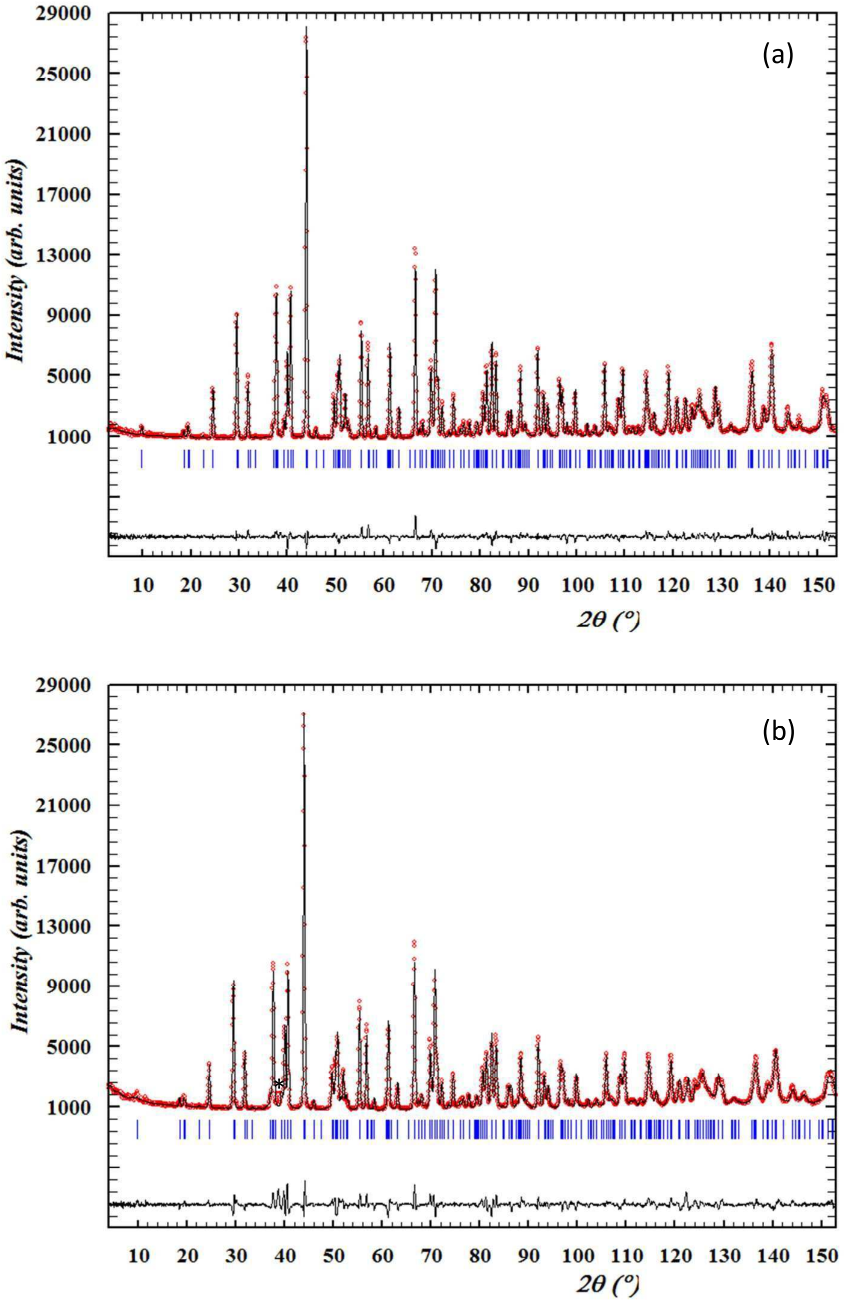

Fig. 3. Observed (circles), calculated (continuous line) and difference (continuous line at bottom) neutron powder diffraction profiles of (a) $Sr_3NdNb_3O_{12}$ and (b) $Sr_3NdNb_{2.94}Ti_{0.06}O_{12-\delta}$. Vertical bars indicate the expected position of Bragg peaks. The presence of a Nb parasite peak arising from the experimental set-up is indicated in Fig. 3(b).

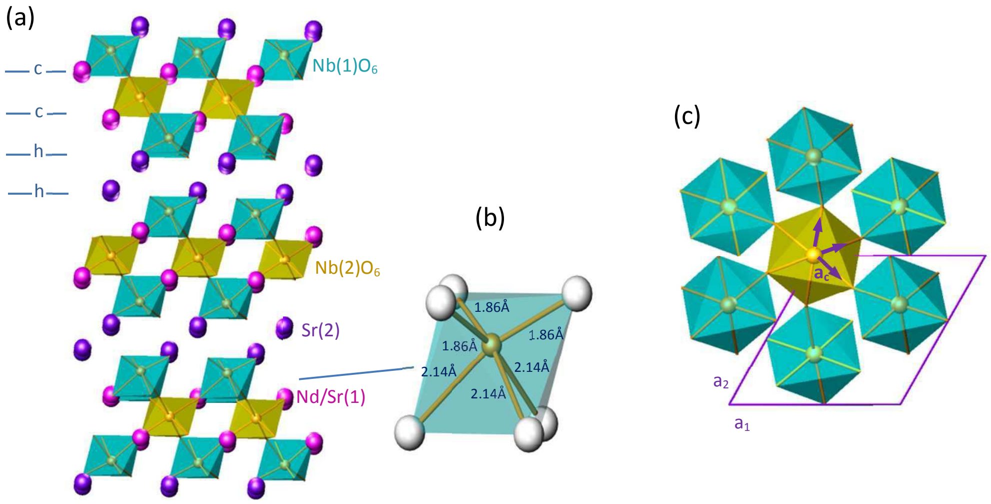

Fig. 4. Schematic diagrams of the $Sr_3NdNb_3O_{12}$ structure: (a) projection down the [1 0 0] zone axis, showing hhcc stacking sequence of $AO_3$ layers; (b) representation of Nb(1)$O_6$ octahedron showing displacement of Nb towards a cation-site vacancy; (c) projection down the [0 0 1] zone axis showing octahedral tilting according to the $a^-a^-a^-$ tilt system along the pseudo-cubic cell directions.

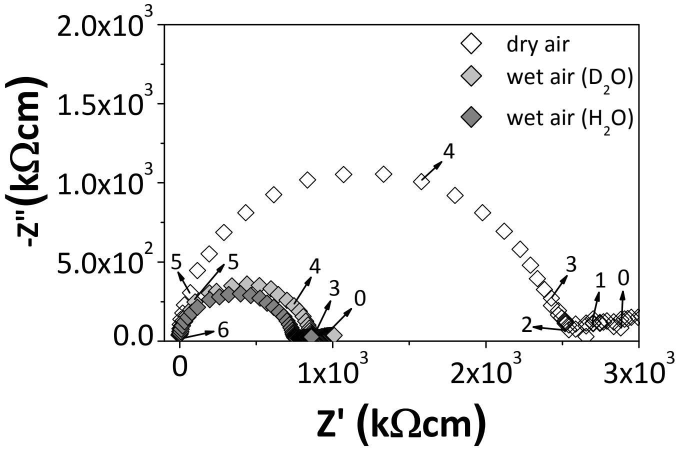

Fig. 5. Impedance spectra of $Sr_3NdNb_3O_{12}$ in dry and humidified air at 700 °C (numbers refer to the approximate value of $\log_{10}$ of the frequency in Hz).

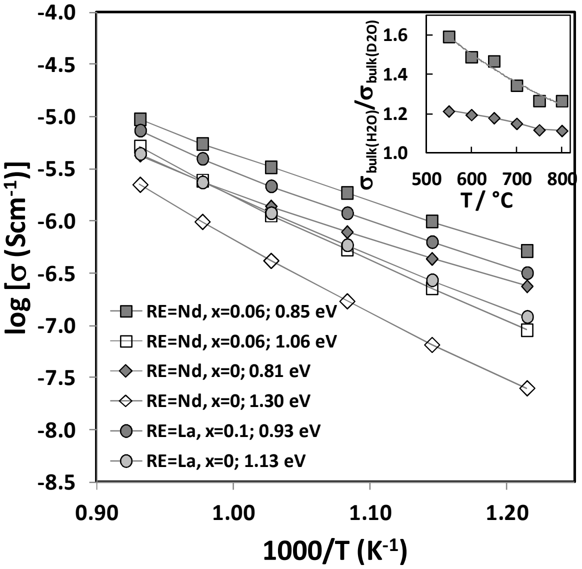

Fig. 6. Temperature dependencies of the bulk conductivity of the series $Sr_3NdNb_{3-x}Ti_xO_{12-\delta}$ and $Sr_3LaNb_{3-x}Ti_xO_{12-\delta}$ (from ref. [8]) in dry and wet air shown with open and shaded symbols, respectively. The inset shows the magnitude of the conductive isotope effect for x = 0 and 0.6 members of the Nd-containing series as a function of temperature employing conductivity data collected in $D_2O$-wetted air.

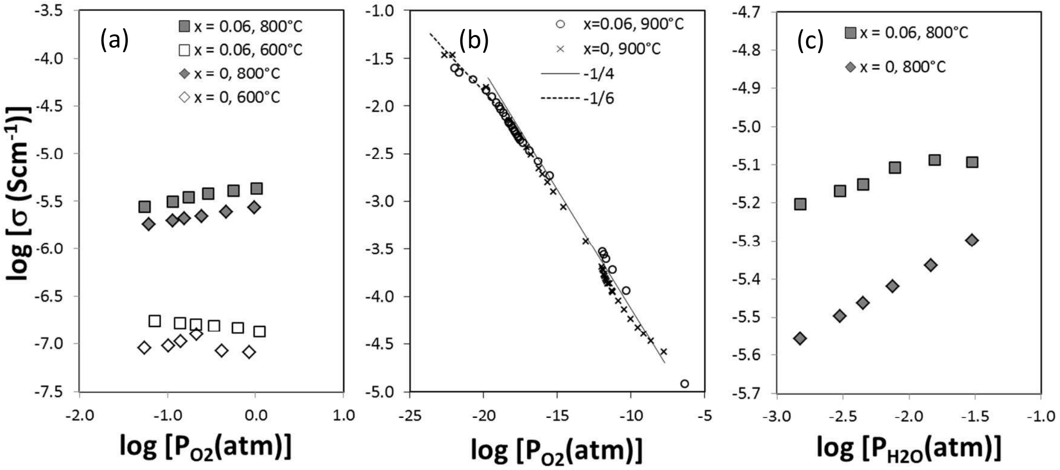

Fig. 7. Selected partial-pressure dependencies of electrical conductivity for $Sr_3NdNb_{3-x}Ti_xO_{12-\delta}$ (x = 0 and 0.06): (a) bulk conductivity as a function of $pO_2$ in dry oxidising conditions; (b) total conductivity as a function of $pO_2$ in reducing conditions; (c) bulk conductivity as a function of $pH_2O$ in oxidising atmosphere.

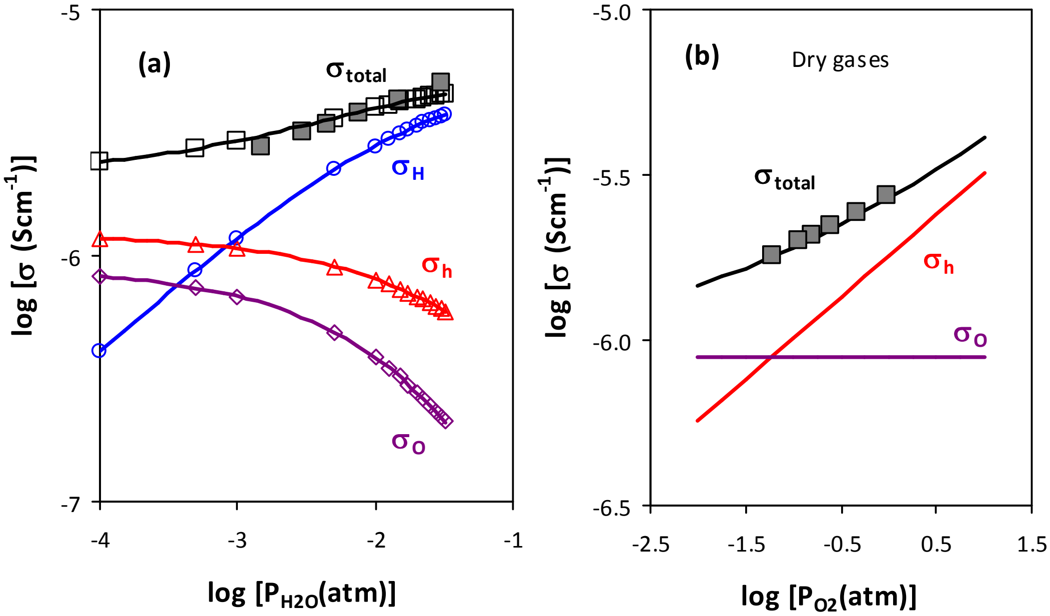

Fig. 8. Simulated conductivity of transport carriers and total conductivity as a function of $pH_2O$ (a) and $pO_2$ (b) and comparison with the experimental results of total conductivity (closed squares) for $Sr_3NdNb_3O_{12-\delta}$.

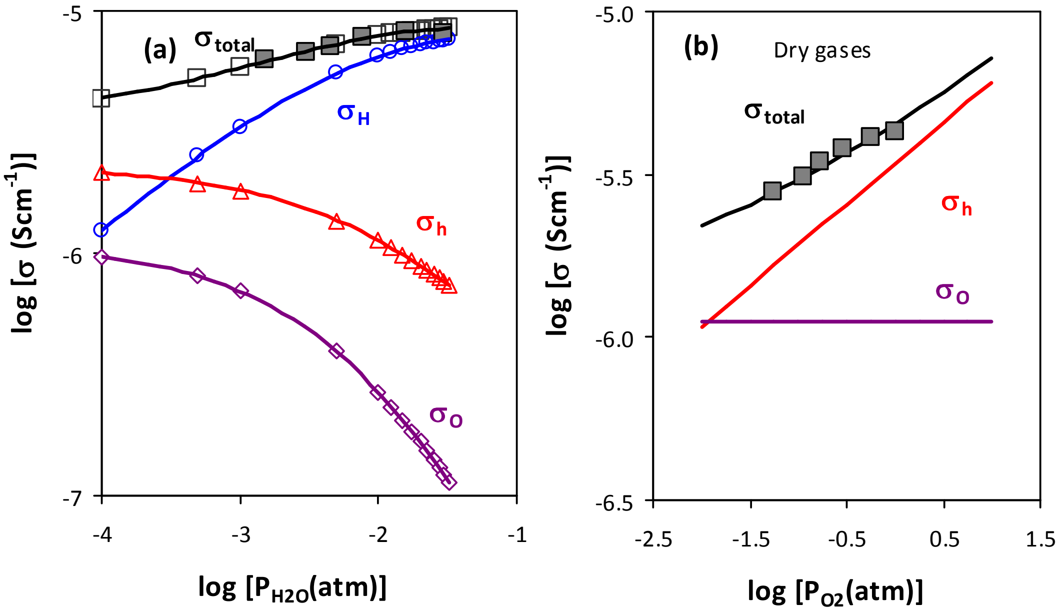

Fig. 9. Simulated conductivity profiles of transport species and total conductivity as a function of (a) $pH_2O$ and (b) $pO_2$ showing fit with the experimental results of total conductivity (closed squares) for $Sr_3NdNb_{2.94}Ti_{0.06}O_{12-\delta}$.

The solid solution $Sr_3NdNb_{3-x}Ti_xO_{12-\delta}$ ($0 \leq x \leq 0.06$) crystallises with a 12R-type hexagonal perovskite structure and exhibits increasing proton conductivity with x.